Facile and Large-scale Synthesis of Defective Black TiO$_{2-x}$(B) Nanosheets for Efficient Visible-light-driven Photocatalytic Hydrogen Evolution

JingCheng Xu †, **JiaJia Zhang** †, **ZhengYang Cai, He Huang, TianHao Huang, Ping Wang** * and **XianYing Wang**

School of Materials Science and Technology, University of Shanghai for Science and Technology, Jungong Rd.516, Shanghai 200093, China; jchxu@usst.edu.cn (J.X.); zhangjiajia2059@outlook.com (J.Z.); Zhengyang_Cai@outlook.com (Z.C.); hh67750@outlook.com (H.H.); tianhaohuang1997@outlook.com (T.H.); xianyingwang@usst.edu.cn (X.W.)

* Correspondence: ping.wang@usst.edu.cn
† These authors contributed equally to the work.

check for updates

Abstract: In the work, we firstly report the facile and large-scale synthesis of defective black TiO$_{2-x}$(B) nanosheets via a dual-zone NaBH$_4$ reduction method. The structure, physico-chemical, and optical properties of TiO$_{2-x}$(B) nanosheets were systematically characterized by powder X-ray diffraction, Raman spectroscopy, UV-Vis absorption spectroscopy, and X-ray photoelectron spectroscopy, etc. The concentration of Ti^{3+} can be well tuned by NaBH$_4$ reduction. With increasing the mass ratio of NaBH$_4$ to TiO$_2$(B), the generation of Ti^{3+} defects gives rise to the increased intensity of a broad band absorption in the visible wavelength range. It is demonstrated that the TiO$_{2-x}$(B) photocatalyst synthesized with the mass ratio of NaBH$_4$ to TiO$_2$(B) of 3:1 exhibited an optimum photocatalytic activity and excellent photostability for hydrogen evolution under visible-light irradiation. By combining the advantages of 2D TiO$_2$(B) nanosheets architecture with those of Ti^{3+} self-doping and simultaneous production of oxygen vacancy sites, the enhanced photocatalytic performance of the defective TiO$_{2-x}$(B) nanosheets was achieved.

Keywords: photocatalysis; photoreforming; hydrogen evolution; black titanium; defects

1. Introduction

Photocatalytic semiconducting materials for hydrogen evolution via water splitting have attracted considerable interest [1–4]. The anatase-, rutile-, and brookite-type TiO$_2$ are the most widely studied photocatalysts. However, their potential applications are hindered severely by their large band gaps and consequently their limited visible-light-harvesting properties. Therefore, several approaches to enhance visible-light photoactivity and inhibit charge carrier recombination in TiO$_2$-based photocatalysis have been developed, such as co-catalysts deposition [5,6], hetero/self-doping [7–10], junction composite [11,12], crystal facet engineering [13,14], surface disordering [15,16], etc. Especially, the intrinsic defects in the TiO$_2$ matrix have been proved to trigger the visible-light activity of TiO$_2$ [17–22]. The hydrogenation-induced defect-rich black TiO$_{2-x}$ displays remarkable stability and photoactivity. Meanwhile, the theoretical results also clearly demonstrate that a vacancy band state is formed as a result of the high vacancy concentration, thus achieving a narrow band gap (about 1.0 eV).

Apart from these TiO$_2$ polymorphs, the crystalline structure of the metastable TiO$_2$(B) nanosheet is found to be a layered and perovskite-like with lattice channels. The synthesis process is facile with ethylene glycol solutions and 140–180 °C, and only involves a one-step hydrolysis reaction of TiCl$_3$ or

TiCl$_4$ [23,24]. Therefore, extensive efforts have been contributed to investigate the applications of the TiO$_2$(B) nanosheet in the photocatalysis field [23,25–28]. However, due to the metastable structure and character of TiO$_2$(B), almost no work has been reported on the facile and large-scale synthesis method and concurrently controllable structure and optical properties for defect-rich TiO$_{2-x}$(B).

In this paper, we offer a facile dual-zone reduction approach to produce defect-rich TiO$_{2-x}$(B) nanosheets by using NaBH$_4$ as reductant agents. By adjusting the mass ratio of NaBH$_4$/TiO$_2$(B), the formation of Ti^{3+} and oxygen-vacancy defects can be well controlled. The as-synthesized defective TiO$_{2-x}$(B) exhibited a broad absorption in the visible-light range, achieving the visible-light photoactivity for H$_2$ evolution.

2. Results and Discussions

2.1. Fabrication of Defective Black TiO$_{2-x}$(B) Nanosheets

The TiO$_2$(B) phase commonly suffers from phase transformation into the stable TiO$_2$ phase (anatase or rutile) in high-temperature annealing conditions, owing to the thermodynamically metastable structure. Thus, this work provides a new and simple dual-zone NaBH$_4$ reduction approach to produce defective TiO$_{2-x}$(B) nanosheets (Figure 1), showing the potential to replace the dangerous high-temperature hydrogenation method by directly using H$_2$ as reductant reagent. Moreover, the byproducts residues from decomposition reactions of NaBH$_4$ can be also avoided. Taking the advantage of the dual-zone reduction synthetic procedure, the phase transformation of TiO$_2$(B) was inhibited, achieving self-doping of Ti^{3+} and simultaneous formation of oxygen vacancy sites.
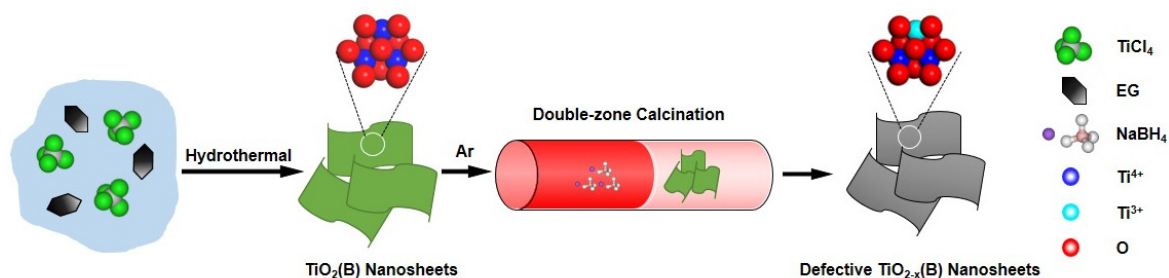

Figure 1. Schematic illustration for the formation of defective black TiO$_{2-x}$(B) nanosheets.

2.2. Material Characterizations

Figure 2 shows the powder XRD patterns of the defective TiO$_{2-x}$ samples. The observed diffraction peaks at 2θ = 25.0°, 28.6°, and 48.6° can be assigned to the [110], [002], and [020] planes of the TiO$_2$(B) phase (JCPDS No.74-1940), indicating that no phase transformation was observed on the as-synthesized TiO$_{2-x}$(B) samples. The results show that under the mild reduction conditions, the simultaneous self-doping of Ti^{3+} and generation of oxygen vacancy sites were achieved, thus inhibiting the phase transformation of TiO$_2$(B). In addition, the diffraction peaks intensity was decreased, not only indicating the decreased crystallinity of TiO$_{2-x}$(B) along with increasing the mass ratio of NaBH$_4$ to TiO$_2$(B), but also shows that the TiO$_2$(B) prepared by simple hydrothermal method possesses a low crystallinity and the reduction process at 200 °C further reduces the crystallinity.

Raman scatterings (shown as Figure 3) were measured to further examine the structure of the obtained TiO$_{2-x}$(B) samples. No obvious change was observed on the Raman spectra of the as-synthesized TiO$_{2-x}$(B) samples. However, with increasing the mass ratio of NaBH$_4$ to TiO$_2$(B), an obvious decrease in the Raman signal intensity was observed, indicating the lower crystallinity of the TiO$_2$(B) phase, which is consistent with XRD results.
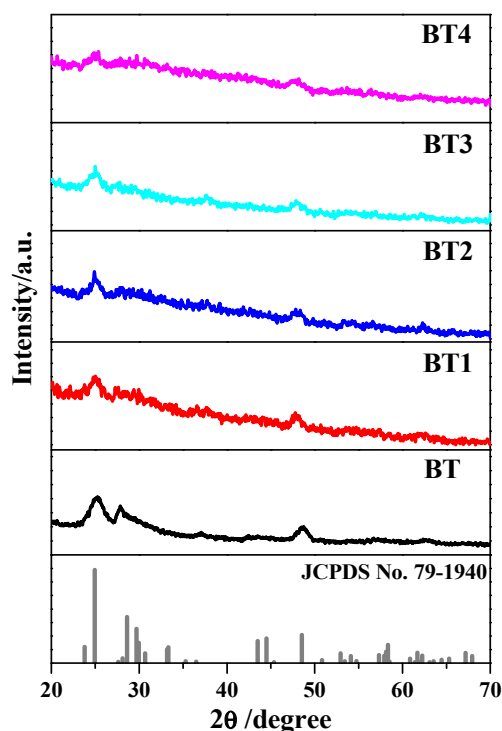
Figure 2. Powder XRD patterns of the as-synthesized pristine $TiO_2(B)$ and defective $TiO_{2-x}(B)$ nanosheets.

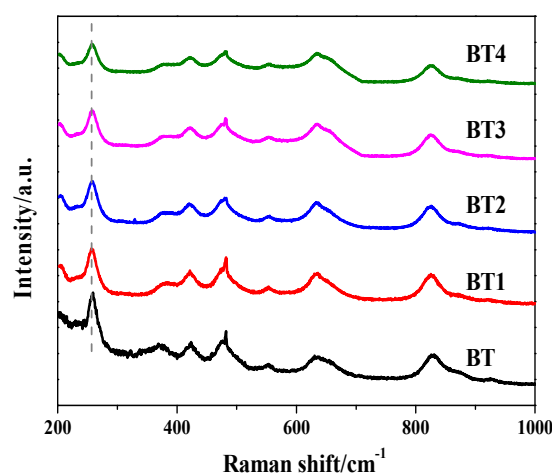**Figure 3.** Raman spectra of defective $TiO_{2-x}(B)$ nanosheets in comparison to that of pristine $TiO_2(B)$.

Figure 4 shows the UV-Vis absorption spectra (a) and Tauc plots (b) for the defective $TiO_{2-x}(B)$ nanosheets compared to the pristine $TiO_2(B)$. It can be seen that, with increasing the mass ratio of $NaBH_4$ to $TiO_2(B)$, the UV-Vis absorption of defective $TiO_{2-x}(B)$ samples is enhanced to expand to the entire visible-light region, in accordance with distinct color change from white BT into black BT3 (inset of Figure 4b).The results confirm the assumption that a new vacancy band state, located below the conduction band minimum (CBM) of $TiO_2(B)$, can be formed by high concentration of Ti^{3+} doping. [17]

As shown in Figure 5a, the XPS survey spectra show the similar surface components of Ti and O elements in BT and BT3. The narrow scan XPS spectra of Ti 2p show that the binding energies of the spin doublet with Ti $2p_{3/2}$ and $2p_{1/2}$ are 458.4 and 464.1 eV, respectively (Figure 5b). The result indicates that the Ti species mainly exist as Ti^{4+}, which is in good accordance with the literature results [29]. Moreover, the devolution of the Ti 2p XPS spectrum for the BT3 sample results in the obvious peaks

belonging to Ti^{3+}, for which the Ti 2p$_{1/2}$ and Ti 2p$_{3/2}$ peaks are located at about 457.5 and 463.2 eV, which confirms the generation of surface Ti^{3+} in TiO$_2$(B). Such differences can be ascribed to the reduction of Ti^{4+} into Ti^{3+} after the NaBH$_4$ treatment. As represented in Figure 5c, the deconvoluted peaks of O1s at 529.7, 531.0, and 532.8 eV are due to the lattice oxygen (Ti–O–Ti), surface hydroxyl group/O–defective matrix (Ti–O–H), and Ti–O–C groups, respectively [30–32]. The observation of Ti–O–C groups can be attributed to the surface-absorbed ethylene glycolate [26]. More interesting, the amount of lattice Ti–O–Ti bonds relative to surface Ti–O–H bonds/O–defective matrix was notably increased in BT3, as compared to those of BT. The results indicate the simultaneous production of oxygen vacancy sites [26,32].
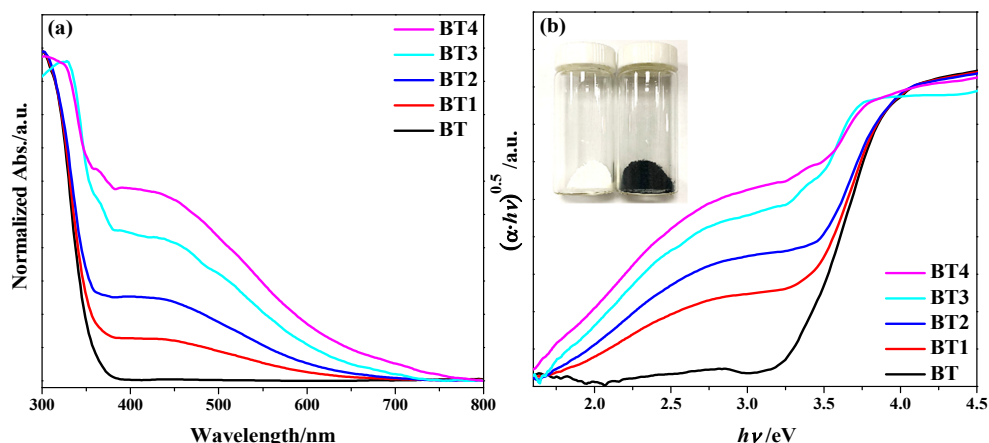

Figure 4. UV-Vis absorption spectra (**a**) and Tauc plots (**b**) of pristine TiO$_2$(B) and defective TiO$_{2-x}$(B) nanosheets. Inset of (**b**), distinct color change from white BT to black BT3.
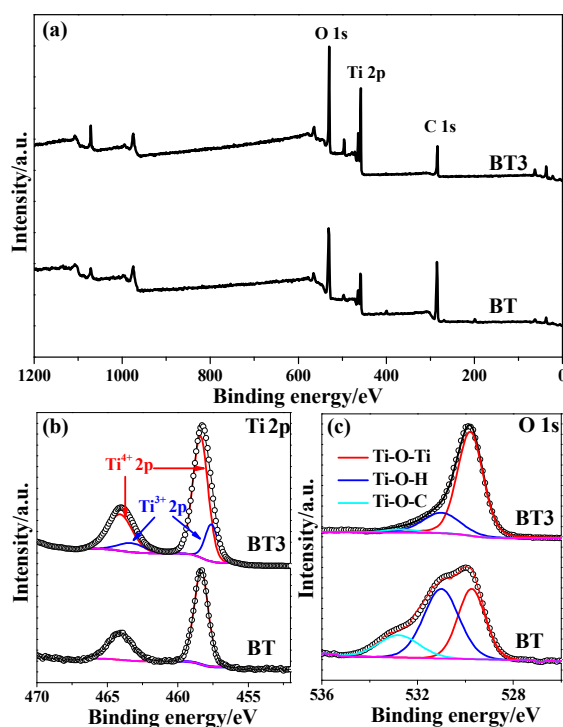

Figure 5. XPS spectra of pristine TiO$_2$(B) and defective TiO$_{2-x}$(B): Survey scans (**a**), narrow scan Ti 2p (**b**), narrow scan O 1s (**c**).

2.3. Photocatalytic Activity for H$_2$ Evolution

The amounts and rates of H$_2$ evolution from aqueous methanol solution under visible-light were measured to represent the photocatalytic activity of the defect-containing TiO$_{2-x}$(B) with photodeposition of 0.03 wt.% Rh as co-catalysts, as shown in Figure 6. No H$_2$ gases were evolved from pristine BT. Interestingly, by an intermittent visible-light irradiation (every 30 min radiation followed by 30 min interval), the stable and continuous H$_2$ evolution (nearly linear correlation between the evolved hydrogen amount with the irradiation time) was observed on the as-synthesized defective TiO$_{2-x}$(B) samples (Figure 6a), indicating no significant deactivation of H$_2$ evolution and excellent stability of defective TiO$_{2-x}$(B) nanosheets. With increasing the mass ratio of NaBH$_4$/BT, the H$_2$ evolution from BT1 increased drastically, reached the maximum average rate of 0.58 μmol·g^{-1}·h^{-1} for BT3, and then decreased (Figure 6b). The results confirm that the appropriate amount of self-doped Ti^{3+} defects along with the production oxygen vacancy sites are the key factors, leading to enhanced photocatalytic performance of the defective TiO$_{2-x}$(B) nanosheets.
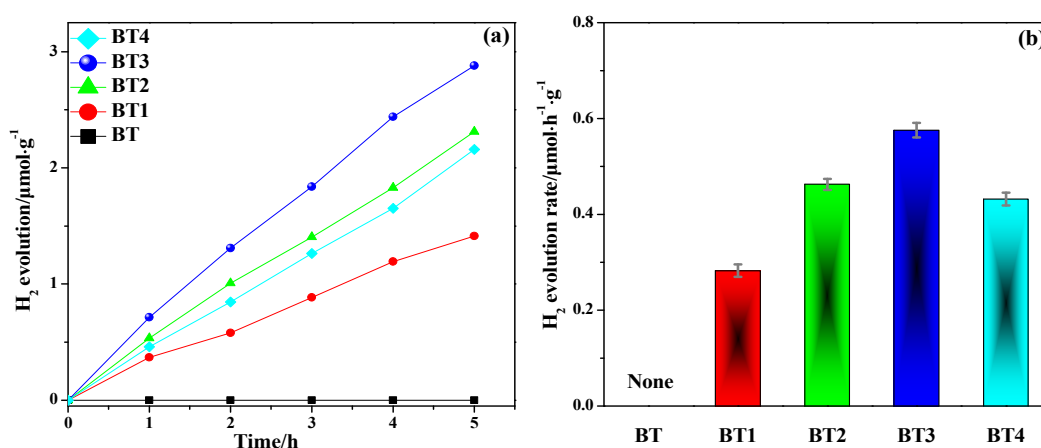

Figure 6. (**a**) Photocatalytic H$_2$ evolution over the as-synthesized defective TiO$_{2-x}$(B) nanosheets under visible-light irradiation (>420 nm) and reaction conditions—0.03 g of catalysts, 30 mL of 10 vol.% aqueous methanol solution, loading of 0.03 wt.% Rh as co-catalysts. (**b**) The corresponding average H$_2$ evolution rates of the as-synthesized defective TiO$_{2-x}$(B). Error bars are generated by measurements repeated at least three times for all samples, with less than 5% deviations for the samples prepared in different batches.

3. Experimental

3.1. Chemicals

Titanium tetrachloride (TiCl$_4$, ≥99%) and Na$_3$RhCl$_6$ were purchased from Alfa Aesar. Ethylene glycol (EG, ≥99%), sodium borohydride (NaBH$_4$, ≥99%), and methanol (MeOH, ≥99.9%) were purchased from Sigma-Aldrich.

3.2. Photocatalysts Preparation

A modified hydrolysis method was used to synthesize the TiO$_2$(B) nanosheet powders [23]. Typically, a desired amount of deionized water was added into the pre-mixture of TiCl$_4$ and ethylene glycol, and then heated at 150 °C for 6 h in a Teflon-lined stainless-steel autoclave. Finally, centrifugation, washing by deionized water and ethanol, and drying at 80 °C all night were performed to obtain products (denoted as BT).

The BT as precursor and the NaBH$_4$ as reductant agent at different mass ratios of 1 to 4 were separately placed in a dual-zone quartz tube furnace. The reduction processes were carried out in an argon atmosphere with a flow rate of 10 mL/min (5.0 quality) at a heating rate of 5 °C/min. The NaBH$_4$ and BT samples were annealed at 500 and 200 °C for 1 h, respectively. After being cooled to room

temperature, the samples were thoroughly washed with deionized water and ethanol several times, and dried at 80 °C overnight. The obtained products were accordingly denoted as BT1, BT2, BT3, and BT4, with respect to the different mass ratio of 1 and 4.

3.3. Characterization

The X-ray diffraction (XRD) patterns of all samples were recorded using a PANalytical MPD diffractometer, with the radiation source of Cu-Kα (λ = 0.1541 nm) X-ray emission, and the scan range was set to 10° to 70° (2θ), with step of 0.05°. Raman spectra of all samples were collected using a Renishaw Raman microscope equipped with a 514 nm excitation laser. Taking BaSO$_4$ as a reference, the UV-Vis absorption spectra were measured using a Shimadzu UV-2450 spectrophotometer. The X-ray photoelectron spectroscopy (XPS) measurements were carried out in Thermo ESCALAB 250XI System (ThermoFisher Scientific, Waltham, MA, USA), consisting of the Mg-Kα X-ray radiation source (*hν* = 1253.6 eV) operating at 250 W (14 kV) and a high resolution hemisphere energy analyzer.

The base pressure of about 5×10^{-10} mbar was maintained in the measurement chamber. To obtain an overall energy resolution of 0.25 eV, the fixed transmission mode and pass energy of 93.9 eV were adopted during the measurements. The charging effects were compensated by a flood gun. A piece of carbon tape (Nisshin EM Co. Ltd, Tokyo, Japan) was used to manually mount samples in the sample holder. The XPS peak deconvolution was performed using the Casa software (Version 2.3.15 RUB license, Casa Software Ltd, Teignmouth, UK, 2009) with Shirley background subtraction and Gaussian–Lorentzian broadening function.

3.4. Photocatalytic Activity Tests

Photocatalytic hydrogen production reactions were conducted in a homemade eight-parallel multi-zone reaction system with air-tight quartz reactors. A 500 W mid-pressure Hg lamp was equipped as light irradiation source, with a water filter and a 420 nm cut-off filter. The evolved gases were determined by gas chromatography method using a thermal conductivity detector (GC7900, Techcomp Ltd., Beijing, China, MS-5A column and high-purity N$_2$ (5.0 quality) as carrier gas). Typically, 30 mg powders were dispersed in 30 mL 10 vol.% aqueous methanol solution (MeOH), and then the ultrasonication was carried out for 10 min. Subsequently, for in-situ photodeposition of optimum amount of 0.03 wt.% Rh as co-catalyst, the Na$_3$RhCl$_6$ solution was added as precursor. Before irradiation, including the photocatalysts, the whole system was purged with N$_2$ (5.0 quality) to remove air completely.

4. Conclusions

In summary, a facile and large-scale approach of a dual-zone NaBH$_4$ reduction method was used for preparing defective black TiO$_{2-x}$(B) nanosheets. We demonstrate that the mass ratio of NaBH$_4$ to TiO$_2$(B) plays a critical role in controlling the self-doped Ti^{3+} defects and simultaneously produced oxygen vacancy sites towards engineering the defective TiO$_{2-x}$(B). The presence of Ti^{3+} and oxygen vacancy defects gives rise to the significantly increased intensity of the broad band absorption in the visible wavelength range. Under visible-light irradiation, the photocatalytic performance of defective TiO$_{2-x}$(B) photocatalysts was greatly enhanced with excellent stability for hydrogen evolution, as compared to the non-photoactive pristine TiO$_2$(B). The synthetic approach for synthesis of defective TiO$_{2-x}$(B) shows great significance for developing a highly efficient catalytic system.

Author Contributions: Design of experiments and preparation and review of original manuscript were performed by J.X., J.Z., P.W., Z.C., H.H. and T.H.; supervision, final reviewing, and editing acquisition were performed by J.X., P.W. and X.W. All authors discussed the results and contributed to the final manuscript.

References

1. Yang, P.; Tarascon, J.M. Towards systems materials engineering. *Nat. Mater.* **2012**, *11*, 560–563. [CrossRef] [PubMed]

2. Bard, A.J.; Fox, M.A. Artificial Photosynthesis: Solar Splitting of Water to Hydrogen and Oxygen. *Acc. Chem. Res.* **1995**, *28*, 141–145. [CrossRef]

3. Wang, P.; Chen, P.; Kostka, A.; Marschall, R.; Wark, M. Control of Phase Coexistence in Calcium Tantalate Composite Photocatalysts for Highly Efficient Hydrogen Production. *Chem. Mater.* **2013**, *25*, 4739–4745. [CrossRef]

4. Zhan, W.; Sun, L.; Han, X. Recent Progress on Engineering Highly Efficient Porous Semiconductor Photocatalysts Derived from Metal–Organic Frameworks. *Nano-Micro Lett.* **2019**, *11*, 1. [CrossRef]

5. Ai, G.; Mo, R.; Li, H.; Zhong, J. Cobalt phosphate modified TiO_2 nanowire arrays as co-catalysts for solar water splitting. *Nanoscale* **2015**, *7*, 6722–6728. [CrossRef]

6. Yang, J.; Wang, D.; Han, H.; Li, C. Roles of Cocatalysts in Photocatalysis and Photoelectrocatalysis. *Acc. Chem. Res.* **2013**, *46*, 1900–1909. [CrossRef]

7. Asahi, R.; Morikawa, T.; Ohwaki, T.; Aoki, K.; Taga, Y. Visible-light photocatalysis in nitrogen-doped titanium oxides. *Science* **2001**, *293*, 269–271. [CrossRef]

8. Zhang, Y.; Xing, Z.; Liu, X.; Li, Z.; Wu, X.; Jiang, J.; Li, M.; Zhu, Q.; Zhou, W. Ti^{3+} Self-Doped Blue TiO_2(B) Single-Crystalline Nanorods for Efficient Solar-Driven Photocatalytic Performance. *ACS Appl. Mater. Interfaces* **2016**, *8*, 26851–26859. [CrossRef]

9. Ran, P.; Jiang, L.; Li, X.; Zuo, P.; Li, B.; Li, X.; Cheng, X.; Zhang, J.; Lu, Y. Redox shuttle enhances nonthermal femtosecond two-photon self-doping of rGO–TiO_{2-x} photocatalysts under visible light. *J. Mater. Chem.* **2018**, *6*, 16430–16438. [CrossRef]

10. Choi, J.; Park, H.; Hoffmann, M.R. Effects of Single Metal-Ion Doping on the Visible-Light Photoreactivity of TiO_2. *J. Phys. Chem. C* **2010**, *114*, 783–792. [CrossRef]

11. Sun, B.; Zhou, W.; Li, H.; Ren, L.; Qiao, P.; Li, W.; Fu, H. Synthesis of Particulate Hierarchical Tandem Heterojunctions toward Optimized Photocatalytic Hydrogen Production. *Adv. Mater.* **2018**, *30*, 1804282. [CrossRef] [PubMed]

12. Marschall, R. Semiconductor Composites: Strategies for Enhancing Charge Carrier Separation to Improve Photocatalytic Activity. *Adv. Funct. Mater.* **2014**, *24*, 2421–2440. [CrossRef]

13. Liu, G.; Yu, J.C.; Lu, G.Q.; Cheng, H. Crystal facet engineering of semiconductor photocatalysts: Motivations, advances and unique properties. *Chem. Commun.* **2011**, *47*, 6763–6783. [CrossRef] [PubMed]

14. Liu, S.; Yu, J.; Jaroniec, M. Anatase TiO_2 with Dominant High-Energy {001} Facets: Synthesis, Properties, and Applications. *Chem. Mater.* **2011**, *23*, 4085–4093. [CrossRef]

15. Zhou, W.; Li, W.; Wang, J.; Qu, Y.; Yang, Y.; Xie, Y.; Zhang, K.; Wang, L.; Fu, H.; Zhao, D. Ordered Mesoporous Black TiO_2 as Highly Efficient Hydrogen Evolution Photocatalyst. *J. Am. Chem. Soc.* **2014**, *136*, 9280–9283. [CrossRef] [PubMed]

16. Chen, X.; Liu, L.; Huang, F. Black titanium dioxide (TiO_2) nanomaterials. *Chem. Soc. Rev.* **2015**, *44*, 1861–1885. [CrossRef] [PubMed]

17. Fang, W.; Xing, M.; Zhang, J. A new approach to prepare Ti^{3+} self-doped TiO_2 via NaBH4 reduction and hydrochloric acid treatment. *Appl. Catal. B Environ.* **2014**, *160–161*, 240–246. [CrossRef]

18. Chen, X.; Lei, L.; Yu, P.Y.; Mao, S.S. Increasing Solar Absorption for Photocatalysis with Black Hydrogenated Titanium Dioxide Nanocrystals. *Science* **2011**, *331*, 746–750. [CrossRef]

19. Ullattil, S.G.; Periyat, P. A 'one pot'gel combustion strategy towards Ti^{3+} self-doped 'black'anatase TiO_{2-x} solar photocatalyst. *J. Mater. Chem. A* **2016**, *4*, 5854–5858. [CrossRef]

20. Santara, B.; Giri, P.; Imakita, K.; Fujii, M. Evidence for Ti interstitial induced extended visible absorption and near infrared photoluminescence from undoped TiO_2 nanoribbons: An in situ photoluminescence study. *J. Phys. Chem. C* **2013**, *117*, 23402–23411. [CrossRef]

21.   Naldoni, A.; Altomare, M.; Zoppellaro, G.; Liu, N.; Kment, S.; Zboril, R.; Schmuki, P. Photocatalysis with reduced TiO$_2$: From black TiO$_2$ to cocatalyst-free hydrogen production. *ACS Catal.* **2018**, *9*, 345–364. [CrossRef] [PubMed]

22.   Kumaravel, V.; Mathew, S.; Bartlett, J.; Pillai, S.C. Photocatalytic hydrogen production using metal doped TiO$_2$: A review of recent advances. *Appl. Catal. B Environ.* **2018**, *244*, 1021–1064. [CrossRef]

23.   Xiang, G.; Li, T.; Zhuang, J.; Wang, X. Large-scale synthesis of metastable TiO$_2$(B) nanosheets with atomic thickness and their photocatalytic properties. *Chem. Commun.* **2010**, *46*, 6801–6803. [CrossRef] [PubMed]

24.   Zhenyu, S.; Xing, H.; Martin, M.; Wolfgang, S.; Edgar, V. A carbon-coated TiO$_2$(B) nanosheet composite for lithium ion batteries. *Chem. Commun.* **2014**, *50*, 5506–5509.

25.   Liu, P.; Zhao, Y.; Qin, R.; Mo, S.; Chen, G.; Gu, L.; Chevrier, D.M.; Zhang, P.; Guo, Q.; Zang, D.; et al. Photochemical route for synthesizing atomically dispersed palladium catalysts. *Science* **2016**, *352*, 797–800. [CrossRef]

26.   Wang, P.; Yi, Z.; Zhang, J.; Cai, Z.; Lyu, B.; Yang, J.; Wang, X. In-situ photosynthetic route to tailor point defects in TiO$_2$(B) nanosheets for visible light-driven photocatalytic hydrogen production. *ChemCatChem* **2019**, *11*, 4252–4255. [CrossRef]

27.   Kong, X.; Xu, Y.; Cui, Z.; Li, Z.; Liang, Y.; Gao, Z.; Zhu, S.; Yang, X. Defect enhances photocatalytic activity of ultrathin TiO$_2$(B) nanosheets for hydrogen production by plasma engraving method. *Appl. Catal. B Environ.* **2018**, *230*, 11–17. [CrossRef]

28.   Wan, N.; Xing, Z.; Kuang, J.; Li, Z.; Yin, J.; Zhu, Q.; Zhou, W. Oxygen vacancy-mediated efficient electron-hole separation for CNS-tridoped single crystal black TiO$_2$(B) nanorods as visible-light-driven photocatalysts. *Appl. Surf. Sci.* **2018**, *457*, 287–294. [CrossRef]

29.   Gai, Z.; Cheng, Z.; Wang, X.; Zhao, L.; Yin, N.; Abah, R.; Zhao, M.; Hong, F.; Yu, Z.; Dou, S. A colossal dielectric constant of an amorphous TiO$_2$:(Nb, In) film with low loss fabrication at room temperature. *J. Mater. Chem. C* **2014**, *2*, 6790–6795. [CrossRef]

30.   Zhang, P.; Shao, C.; Zhang, Z.; Zhang, M.; Mu, J.; Guo, Z.; Liu, Y. TiO$_2$@carbon core/shell nanofibers: Controllable preparation and enhanced visible photocatalytic properties. *Nanoscale* **2011**, *3*, 2943–2949. [CrossRef]

31.   Huang, N.-P.; Michel, R.; Voros, J.; Textor, M.; Hofer, R.; Rossi, A.; Elbert, D.L.; Hubbell, J.A.; Spencer, N.D. Poly (L-lysine)-g-poly (ethylene glycol) layers on metal oxide surfaces: Surface-analytical characterization and resistance to serum and fibrinogen adsorption. *Langmuir* **2001**, *17*, 489–498. [CrossRef]

32.   Das, J.; Pradhan, S.; Sahu, D.; Mishra, D.; Sarangi, S.; Nayak, B.; Verma, S.; Roul, B. Micro-Raman and XPS studies of pure ZnO ceramics. *Phys. B Condens. Matter* **2010**, *405*, 2492–2497. [CrossRef]